Modified synthesis of [Fe/LiF/C] nanocomposite, and its application as conversion cathode material in lithium batteries

Raju Prakash*, Clemens Wall, Ajay Kumar Mishra, Christian Kübel, Mohammad Ghafari, Horst Hahn, Maximilian Fichtner

Karlsruhe Institute of Technology (KIT), Institute of Nanotechnology (INT), Postbox 3640, 76021 Karlsruhe, Germany

ARTICLE INFO

ABSTRACT

In an attempt to enhance the energy storage capacity and discharge voltage, a new cathode material based on ferrocene and LiF for lithium-ion batteries has been explored [Fe/LiF/C] nanocomposite (**1**) has been synthesized by pyrolysis of a ferrocene/LiF mixture at 700 °C using a rotating quartz tube setup in a furnace. The structure and morphology of the composite were investigated by X-ray diffraction (XRD), scanning electron microscopy (SEM), high resolution transmission electron microscopy (HRTEM), Brunauer–Emmer–Teller (BET) analysis, Raman, and Mössbauer spectroscopy. The nanocomposite is composed of well-defined nanotubes which are interlinked by graphitic shell-type structures containing uniformly distribution of Fe, Fe–C, and LiF nanoparticles. The binder-free nanocomposite cathode showed enhanced electrochemical performance with the reversible specific capacity of 230 mAh g^{-1} (1.3–4.3 V) at 20.8 mA g^{-1} at room temperature. It exhibited a remarkable cyclic stability and good rate capability performances. The morphology of **1** was changed by ball milling, and the resulting nanocomposite **2** did not show any cyclic stability as a cathode. Thus, the cyclic stability and rate capability performances of **1** were attributed to its structure and morphology.

1. Introduction

Since the last decade, lithium-ion batteries have dominated commercial applications in a variety of portable electronic devices, as they afford superior performance in terms of energy storage, as well as cyclic stability [1–5]. However, their performance is still low to satisfy the demand for large-scale energy storage applications such as electric vehicles, or power storage from renewable energy resources (solar, wind), etc. [3,6]. These applications essentially require batteries having high energy and power density, rate capability, safety, extended cyclic stability, and low cost [3–6]. As the performance of a battery depends decisively on the properties of the electrode materials [7], the development of new materials that meet the above mentioned requirements is of utmost importance. Currently many oxides and phosphates have been used as cathode materials for rechargeable Li-ion batteries through a Li-ion intercalation process. This process has restricted the reversible reaction to a single electron transfer per formula unit. The specific capacities of the state-of-the-art lithium-ion battery cathodes are currently up to 170 mAh g^{-1}.

Electrochemical conversion reaction seems to be an alternative way to attain a large specific capacity by complete utilization of all the oxidation states of a transition metal compound during the redox cycle [8]. In recent years, a variety of transition metal binary compounds such as oxides [8–10], nitrides [11], sulfides [12] and fluorides [13–21] have been investigated for a large multi-electron redox capacity through reversible conversion reactions. Of these compounds, metal fluorides were the first to be studied as conversion cathode materials (Eq. (1))

$$M^{n+}F_n + ne^- + nLi^+ \rightleftarrows M + nLiF \tag{1}$$

owing to the high operating voltages caused by their high ionic nature. But, the high ionicity of the M–F bond typically induces a wide band gap, which leads to a poor electronic conductivity. As a result, fluoride electrodes suffer greatly from sluggish kinetics. Among metal fluorides, iron fluoride (FeF$_3$) is of particular interest because of its low cost and low toxicity. The electrochemical activity of FeF$_3$ was first reported by Arai et al. with a reversible capacity of 80 mAh g^{-1} in the potential range of 2.5–4.5 V for the Fe^{3+}/Fe^{2+} couple [22]. Later, Badway et al. reported a reversible cathode by forming carbon metal fluoride nanocomposites by high-energy ball milling [13]. The nanosized FeF$_3$ composite displayed a reversible specific capacity as high as 600 mAh g^{-1} for Fe^{3+}/Fe^0 redox couple (theoretical value 712 mAh g^{-1} [23]) at a voltage range of 1.5–4.5 V with a low current density of 7.58 mA g^{-1} at 70 °C [15].

* Corresponding author. Tel.: +49 721 608 28911; fax: +49 721 608 26368.
  E-mail addresses: raju.prakash@kit.edu, rajuprakash@yahoo.com (R. Prakash).

Very recently, Li and coworkers have reported a nanometer-sized $FeF_3 \cdot 0.33H_2O$ cathode prepared by low-temperature ionic liquid based synthesis, which delivered discharge capacities of about 160 and 126 mAh g^{-1} at current densities 14 and 71 mA g^{-1}, respectively [20]. Subsequently, Kang and coworkers have described the establishment of a novel nanoarchitecture CNT–FeF_3 composite (FNCB) [21]. The CNT network was functionalized by formation of FeF_3 nanoflowers on the CNT surfaces. Electrochemical analysis of FNCB electrode exhibited a high capacity of 210 mAh g^{-1} at 20 mA g^{-1} with a voltage range of 1.5–4.5 V at room temperature. Electrochemical studies of FeF_3 systems by other groups [16–19] also suggested that FeF_3 could be a potential candidate for a future cathode material. However, the electrochemical activity of FeF_3 cathode in terms of cyclic stability and rate capability still needs to be improved significantly for practical applications.

Recently we have developed a [Fe/LiF/C] nanocomposite by pyrolysis of a ferrocene/LiF mixture at 700 °C [24,25]. It consists of Fe, Fe_3C and LiF nanoparticles which are intimately mixed in porous multiwalled nanocarbon structures. The composite electrode exhibited reversible capacities of 270 and 170 mAh g^{-1} in the voltage ranges of 0.5–4.3 and 1.3–4.3 V at a current density of 20.8 mA g^{-1} at 20 °C, respectively. In addition, the nanocomposite electrode showed excellent cyclic stability (over 200 cycles) as well as good rate capability. However, this nanocomposite suffered from two major drawbacks: the mixing of the reactive components Fe and LiF was not uniform throughout the composite; secondly, due to low reactivity of Fe_3C towards LiF, a significant amount of LiF was left over in the composite electrode. Herein we report a modified synthesis of a [Fe/LiF/C] nanocomposite (**1**), and its improved electrochemical properties in rechargeable lithium batteries. This composite consists of well-defined nanotubes which are interlinked with nano-granular structure containing a homogeneous mixture of active materials. In addition, we present evidence that the morphology of **1** is crucial for its stable cyclic behavior. For this purpose, [Fe/LiF/C] nanocomposite (**2**) was prepared by ball milling of **1**, and its structural and electrochemical properties were compared with **1**.

2. Experimental

All preparations and manipulations were carried out in an Ar-filled glove box and/or using standard Schlenk techniques. Solvents were dried with appropriate drying agents and distilled prior to use. Ferrocene and lithium fluoride (Alfa Aesar Co.) were dried at 50 and 150 °C for 15 h under vacuum, respectively. In addition, the dried LiF was ball-milled for 20 h (Retsch GmbH; PM400; WC vial/balls; balls: powder ratio = 100:1; 400 rpm) prior to mixing it with ferrocene.

2.1. [Fe/LiF/C] nanocomposite (**1**)

To a solution of ferrocene (1.07 g, 5.7 mmol) in diethyl ether (15 ml), LiF (0.31 g, 12 mmol) was added. The resulting suspension was stirred at 25 °C for 15 min, and then dispersed it in an ultrasonic bath for 15 min. The solvent was removed and the residue was dried in vacuo at 50 °C for 3 h. The homogeneously mixed fine powder was sealed into a stainless steel Swagelok-type reactor (inner diameter, 0.7 cm; length 7 cm) containing vacuum coupling radiation (VCR) type of fittings on both ends. The pyrolysis was performed in a home-made designed rotating furnace setup as shown in Fig. 1. The quartz tube (inner diameter 7 cm, length 75 cm) was placed horizontally inside the tube furnace (GERO) without touching the ceramic wall of the furnace. Both ends of the tube were supported by wheels mounted on top of the Y-shaped rods, while the bottom of the rods connected to an adjustable base plate.

One of the wheels was coupled to a motor (DOGA gear motor, 12 V/DC, 25 rpm, 6 Nm). The reactor was placed in the center of the tube and fixed on both sides with quartz mat. The tube was rotated continuously with a frequency of 10 rpm. Then, the furnace was heated to 700 °C at a temperature ramp of 35 °C min^{-1} (20 min to reach 700 °C) and kept at that temperature for 5 h. During this period, the complete decomposition of ferrocene occurred to form metallic Fe and carbon as major solid products, in addition to various reactive gases. The iron produced acts as catalyst for the growth of nano–tubes/core–shell type structure with the carbon. In addition, iron carbide, an intermediate species, was also formed during this reaction. These components were mixed thoroughly with LiF by using the rotating quartz tube setup to get a homogeneous [Fe/LiF/C] nanocomposite. Then the reactor was allowed to cool down to room temperature naturally without rotation. Due to various gaseous materials produced during pyrolysis, pressure developed inside the reactor. It was opened inside a glove box, and a fine black powder produced was collected (yield: 1.2 g, 91%). Elemental analysis, C 45.3%; EDX: Fe 26.7%, LiF 27.5%.

2.2. Ball-milled [Fe/LiF/C] nanocomposite (**2**)

Composite **1** (500 mg) and pentane (5 ml) were added into a stainless steel vial (80 ml volume) containing balls (SS, balls to powder ratio 50:1). The resulting suspension was milled (Fritsch pulverisette 6) for 4 h at 250 rpm under argon at room temperature. Then, the solvent was removed slowly inside a glove box and the fine powder was collected (yield: 450 mg). Elemental analysis, C 44.5%; EDX: Fe 26.5%, LiF 28.0%.

2.3. Characterization

The phase analyses of the nanocomposites were performed using a Philips X'PERT diffractometer with Cu Kα radiation. PANalytical X'Pert Data Collector and X'Pert HighScore software were used for data acquisition and evaluation, respectively. The samples to be analyzed were spread onto a silicon single crystal in the glove box and sealed with an airtight hood made of Kapton foil, which is out of the focus of the spectrometer. The patterns were recorded at 25 °C in a 2θ range between 10 and 90°. Raman spectra were investigated with a Kaiser optical process spectrometer (RXN1) with an excitation wavelength of 785 nm. Mössbauer spectroscopic measurement was carried out by a constant acceleration-type spectrometer with a ^{57}Co source in a Rh matrix. The samples to be measured were sealed between kapton foils inside a glove box. The isomer shift is given relative to α-Fe at room temperature. The morphology and microstructure of the nanocomposites were investigated using scanning electron microscopy (SEM; Leo-1530) and transmission electron microscopy (TEM; image corrected FEI Titan 80-300 operated at 300 kV in TEM and HAADF-STEM mode, equipped with a Gatan Imaging Filter Tridem 863 and an EDAX s-UTW EDX detector). The sample for TEM analysis was prepared by dispersing the nanocomposite in pentane. A droplet was placed onto a carbon film supported on a copper grid and allowed to dry for at least 2 h. The grids were sealed and reopened to put them into the TEM, thereby minimizing exposure to atmosphere to about a minute. Nitrogen physisorption isotherms were measured using a Micromeritics ASAP 2020 system at 77 K. Prior to measurement, the samples were degassed at 350 °C for 12 h. Pore size distributions (PSD) were calculated based on a DFT model [26] assuming slit-shaped pores. The specific surface area was determined according to the BET theory [27].

Electrochemical properties of the nanocomposites as cathode materials in lithium-ion cells were tested by galvanostatic charge–discharge technique using two-electrode Swagelok-type cells. The nanocomposite powder without any addition of a binder
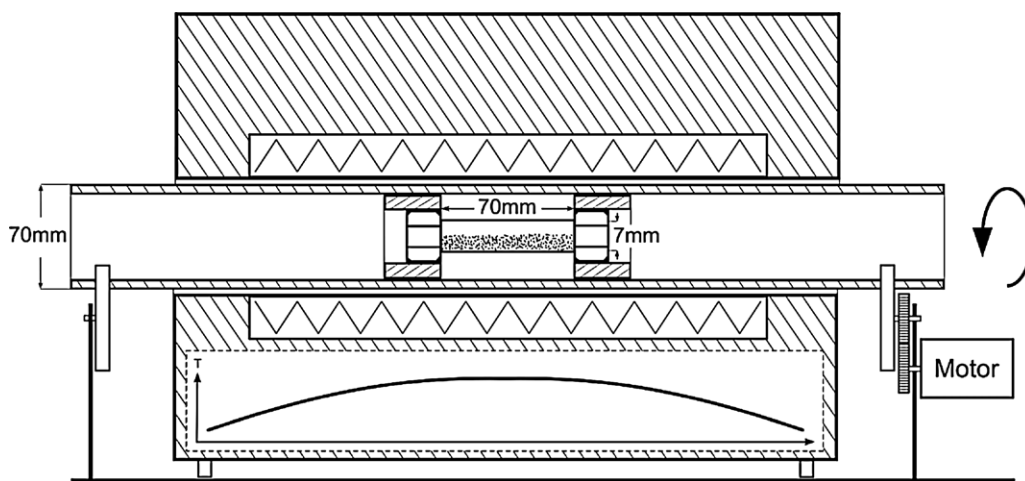
Fig. 1. Rotating quartz tube setup used for the synthesis of nanocomposite **1**.

(because of no significant change in electrochemical performances of the previous [Fe/LiF/C] nanocomposite electrodes, fabricated with or without binder) or carbon (since the nanocomposite consists of carbon more than 40%) was used as test electrode and metallic lithium (Goodfellow) used as reference/counter electrode. Glass fiber (GF/D; Whatman) was used as separator and 1 M LiPF$_6$ in ethylene carbonate (EC) and dimethyl carbonate (DMC) (1:1 v/v) as the electrolyte. Charge/discharge measurements were carried out galvanostatically at various current densities over a voltage range of 1.3–4.3 V (vs. Li/Li$^+$) for 150 cycles using a battery testing system (Arbin Instruments, BT2000 multi-channel system). After 150 charge/discharge cycles, the charged electrode was removed from the cell, washed with anhydrous DMC, dried in vacuo, and then used for further analysis.

3. Results and discussion

[Fe/LiF/C] nanocomposite (**1**) was produced by pyrolysis of a homogeneous mixture of ferrocene and LiF (Fe to LiF ratio of 1:2.2) under Ar at 700 °C for 5 h in the modified furnace shown in Fig. 1. The idea behind the use of such a setup is to mix constantly the components (C/Fe$_3$C/Fe) produced by thermal decomposition of ferrocene and LiF during pyrolysis to get a homogeneous nanocomposite. The amount of carbon present in the nanocomposite was determined by elemental analysis as 45.3 wt%. The relative atomic ratio of Fe and LiF of **1** was estimated by energy dispersive X-rays (EDX) analysis using SEM mode. The ratio of Fe:F was found to be 1:2.2 ± 0.2, thus the amounts of Fe and LiF present in **1** were calculated as 26.7 and 27.5 wt%, respectively.

Fig. 2 shows the XRD pattern of the as-prepared nanocomposite **1**. The diffraction pattern is almost similar to that of the [Fe/LiF/C] nanocomposite synthesized by previous method [24]. All diffraction peaks of **1** can be indexed to four well-defined phases, such as hexagonal phase graphitic carbon {26.3° (0 0 2); JCPDS-041-1487}, cubic phase α-Fe {JCPDS-006-0696}, orthorhombic phase Fe$_3$C {JCPDS-035-0772}, and the cubic phase LiF {JCPDS-004-0857}. Scherrer analyses on the Bragg peaks of Fe (1 1 0), Fe$_3$C (2 1 1), and LiF (2 0 0) have been performed and the approximate crystallite sizes were calculated as 12, 10, and 20 nm, respectively. The major difference in XRD patterns between the previous and the present nanocomposite is the change in observed intensities of α-Fe and Fe$_3$C reflections. In **1**, the intensities of α-Fe peaks at 44.6° (1 1 0), 65.0° (2 0 0) and 82.3° (2 1 1) were increased, while Fe$_3$C peak intensities decreased and more diffused when compared to the intensities of the previous nanocomposite [24]. These results
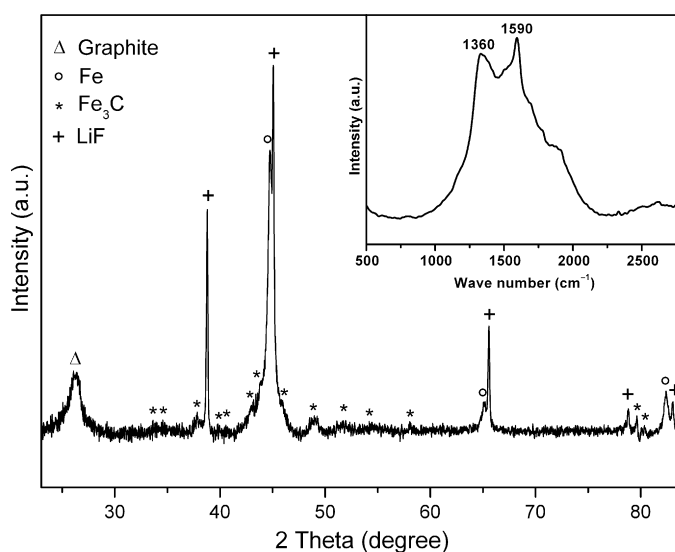

Fig. 2. XRD pattern of nanocomposite **1** formed after pyrolysis of a ferrocene/LiF mixture at 700 °C under argon atmosphere using rotating quartz setup.

suggest that the yield of α-Fe phase in **1** is higher than the cementite Fe$_3$C phase. Since α-Fe phase is the main active species that undergoes conversion reaction readily with LiF to form FeF$_3$, a better electrochemical behavior of **1** can be anticipated. A Raman spectrum of **1** is shown in Fig. 2 inset. It exhibits two bands at 1340 and 1590 cm^{-1}, which are attributed to the D-band (disorder-induced phonon mode [28]) and G-band (graphitic lattice mode E_{2g} [29]) of carbon, respectively. The data revealed that the as-prepared nanocomposite consists of significant amount disordered carbon in addition to highly ordered graphitic carbons.

The Mössbauer spectrum of **1** recorded at room temperature consists of four sub-spectra, three sextets and a doublet (Fig. 3). The sextet with a magnetic hyperfine field of 33.3 T and zero isomer shift corresponds to the hyperfine parameters observed for α-Fe. The second sextet (B_{hf} = 28.5 T and δ = 0.133 mm s^{-1}) corresponds to an amorphous phase of iron-carbon system with a carbon content close to 0.19 atomic percent [30]. Such a phase should exhibit a typical amorphous XRD pattern in between 40° and 50° 2θ [30]. However in the XRD of **1**, it was not possible to clearly distinguish the amorphous phase because its position coincided with positions of more intense peaks of LiF, Fe and Fe$_3$C phases. The third sextet (B_{hf} = 20.8 T and δ = 0.189 mm s^{-1}) and the doublet (Δ = 0.868 mm s^{-1} and δ = 0.189 mm s^{-1}) corresponds to Fe$_3$C [31]
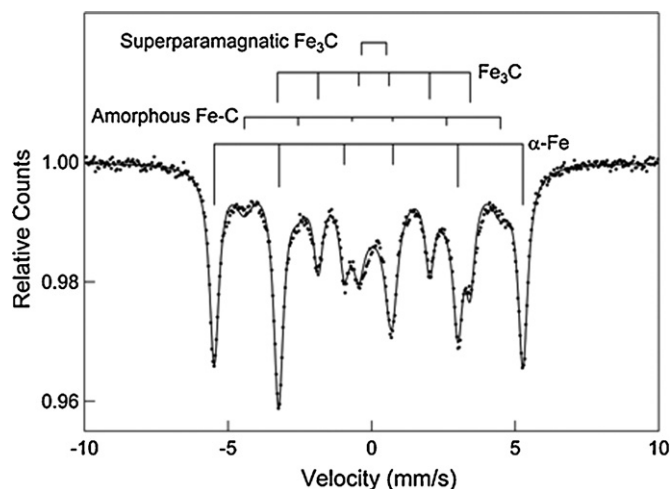
Fig. 3. Mössbauer spectrum of **1** recorded at room temperature. The solid lines are the least square fit to the experimental data in the dotted lines.
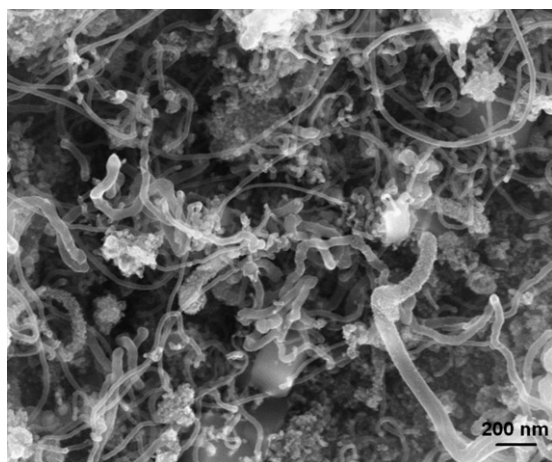

Fig. 4. SEM image of the as-prepared nanocomposite **1**.

with magnetic and super-paramagnetic particles, respectively. The relative areas of Fe, Fe_3C and Fe–C were estimated to be 45, 39 and 16%, respectively. The spectrum of **1** differs mainly from that of the previous nanocomposite [24] in two respects; presence of an iron rich Fe–C phase and a superparamagnetic Fe_3C phase.

The morphology of the material was examined using SEM and TEM. Fig. 4 shows a SEM image of the as-prepared nanocomposite. The sample is composed of entangled carbon nanotubes and nano-granular structures which are closely interlinked with each other. Most of the tubes have lengths on the order of several micrometers and their diameters vary significantly (10–50 nm); a few tubes having diameters of about 100 nm were also observed. A large amount of tubes contain iron-rich nanoparticles, which are embedded at one end while the other end is open. TEM images of the as-prepared composite are shown in Fig. 5. It reveals the existence of two different types of carbon morphologies (nanotubes as well as graphitic onion shells) similar to that of the nanocomposite as reported in our earlier paper [24]. However, the multi-walled tubes produced by this method are well-shaped, and much more extended than those of the nanocomposite synthesized previously. The inner diameters of the multi-walled tubes are ranging from 5 to 30 nm. The high-resolution TEM images indicated that the nano-granular regions consist of core shell-type structure, containing graphitic onions with the characteristic lattice spacings of 0.36 nm in which iron-rich nanoparticles are embedded. Closer inspection of the graphitic

matrix revealed some inhomogeneous onion-like graphitic layers indicating a partial encapsulation of the iron-rich particles by the graphitic matrix.

The HAADF-STEM images indicate a typical diameter of 2–10 nm for the iron-rich particles, but a few particles with up to 50 nm are also observed. The iron-rich particles are either located inside graphitic nanotubes or they are embedded inside onion-like graphite spheres. Like in the original composite, both iron (α-Fe) and iron carbide (Fe_3C) nanocrystals were detected inside the graphitic onions. HAADF-STEM in combination with local EELS/EDX analyses (Fig. 6) revealed carbon, Fe and LiF to be present everywhere in the aggregates. In addition, EDX spectroscopy elemental mapping (by SEM) was used to understand the distribution of C, Fe/Fe_3C and LiF components in the composite. From the elemental distribution of iron, fluorine and carbon (Supplementary information Fig. S1), overall a fairly uniform distribution of Fe/Fe_3C, LiF and carbon in the composite could be recognized. But locally, similar distributions with slightly varying concentrations of elements are observed (Supplementary information Fig. S2). When compared to the synthesis of nanocomposite by using non-rotating and rotating quartz tube methods, the composite obtained by the latter method has a better homogeneous mixture of Fe/LiF/C, and exhibits graphitic carbon morphologies with better electronic conductivities.

The inner surface and porous properties of **1** were investigated by N_2 physisorption analysis. Fig. 7 displays the adsorption–desorption isotherms, pore size distribution and pore volume of nanocomposite **1**. According to IUPAC classification [32], the observed isotherms of **1** can be classified as type-IV absorption branch with an H_3 type hysteresis loop, which is typical for a mesoporous material. In addition, it exhibited a steep increase of the adsorbed gas at very low relative pressures due to presence of micropores (pore width < 2 nm). The sample had micro- and meso-porous volumes of 0.023 and 0.09 $cm^3 g^{-1}$, respectively, and the BET surface area was 130 $m^2 g^{-1}$. The differential pore volume of **1**, calculated from the DFT model [26], suggests that the mesopore sizes were distributed between 5 and 35 nm. When compared to the previous nanocomposite, the mesopore volume of **1** decreased while micropore volume remains unchanged. However, the BET surface area of **1** is significantly larger than that of the previous composite (82 $m^2 g^{-1}$).

The electrochemical performance (specific capacity, cyclic stability and rate capability) of the binder-free [Fe/LiF/C] nanocomposite cathode was evaluated by using galvanostatic cycling at room temperature in two-electrode Swagelok cells with metallic lithium as a negative electrode (Fig. 8). Since carbon has no contribution to the specific capacity in the voltage range between 4.3 and 1.3 V [15–19], the charge and discharge capacities observed from the nanocomposite electrode can directly be ascribed to electroactive Fe/LiF nanoparticles. At first, the cell (OCV: 2.6 V) was charged to 4.3 V at a given current density, and then held at that potential for a calculated period of time which would be necessary to reach its theoretical capacity of 712 $mAh g^{-1}$ galvanostatically. Fig. 8a shows the voltage/specific capacity profiles of the nanocomposite electrode/Li cell cycled between 4.3 and 1.3 V at a current density of 20.8 $mA g^{-1}$. The nanocomposite exhibited a well-defined two-stage discharge with a higher voltage plateau at 3.8–2.5 V, followed by a lower voltage sloped-plateau at 2.3–1.3 V, indicating a two-step reduction process. The charge/discharge features of **1** are similar to those of [Fe/LiF/C] nanocomposite prepared by previous method [24], and to those observed from the ball-milled FeF_3/C nanocomposites at small current drain at room temperature [16–19], or at elevated temperature [15]. The electrochemical reaction (Eq. (1)) proceeds through two successive steps: in the first step, by a one-electron reduction of FeF_3 to form $LiFeF_3$ through a Li insertion reaction, and subsequently, by a two-electron reduction
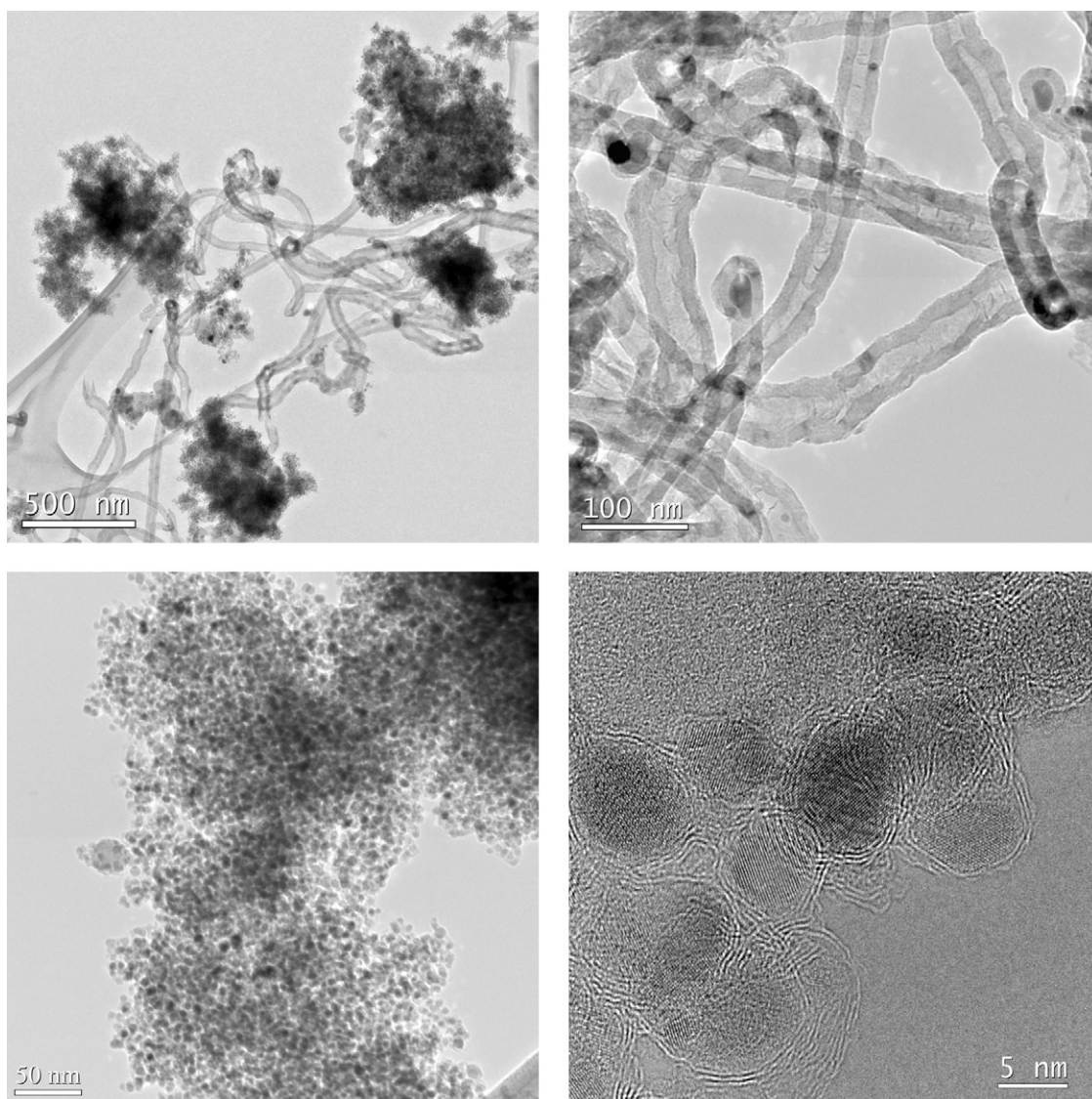
Fig. 5. TEM characterization of the as-prepared [Fe/LiF/C] nanocomposite. Top left: BF-TEM overview image. Top right: iron-rich nanoparticles encapsulated in nanotubes. Bottom left: aggregates of iron-rich nanoparticles confined by onion-like graphitic structures. Bottom right: enlarged view of graphitic coating of the iron-rich particles.

of LiFeF$_3$ to produce Fe and LiF through a conversion reaction, as reported in literature [15–21].

The charge/discharge specific capacities were determined based on the mass of the active material FeF$_3$ (calculated from the amount of Fe and LiF present in **1**). The nanocomposite electrode exhibits first discharge and charge capacities as high as 284 and 256 mAh g^{-1}, respectively. The capacity decreases over the first few cycles and then stabilizes at about 230 mAh g^{-1}. At 150th cycle, the voltage profile did not change much compared to initial cycles, indicating that the cycleability of the cell is very good. The coulombic efficiency of the nanocomposite electrode after the initial few cycles remained close to 100%. The charge/discharge capacities stay stable without any significant capacity fading even up to 150 cycles (Fig. 8b). In order to check the reproducibility of the nanocomposite cathode, six identical cells have been tested galvanostatically under similar conditions for 150 cycles. They exhibited similar performances, within the specific capacity error limit of ±5%. Under identical electrochemical condition, [Fe/LiF/C] nanocomposite obtained by previous method delivered a stable capacity of 170 mAh g^{-1} only [25]. The specific capacity of **1** is very well comparable to the reported capacity (210 mAh g^{-1}) of FNCB electrodes tested at a current rate of 20 mA g^{-1} in the voltage

range between 1.5 and 4.5 V [21]. In order to check the long time stability, one of the six cells was allowed to cycle for more than 150 cycles. The data indicated that the specific capacity remained quite stable up to 200 cycles, and then it decreased gradually. At the end of 400 cycles the capacity was found to 126 mAh g^{-1}, and after 500 cycles it decreased to 68 mAh g^{-1}.

XRD analysis of the charged electrode after 150 cycles showed the phase change of the active materials. The diffraction peaks of Fe had disappeared and LiF decreased significantly, a new reflection peak at 23.6° {FeF$_3$ (0 1 2), JCPDS-033-0674} and a shoulder at 26.8° {FeF$_2$ (1 1 0), JCPDS-045-1062} appeared in the ex situ XRD pattern. Similar to our earlier result [24], the formation of FeF$_2$ phase was observed after several cycles. To know more about the development of the FeF$_2$ phase with cycles, a detailed Mössbauer investigation of the charged electrodes at different cycles is in process.

In order to examine the rate capability of **1**, charge/discharge cycles were performed independently with two identical cells between 1.3 and 4.3 V by varying current densities from 20 to 712 mA g^{-1} at room temperature. The nanocomposite electrode showed rather good rate capability as demonstrated in Fig. 8b. As the current densities increased, the specific capacities decreased, but remained stable over the entire 15 cycles at a given current.
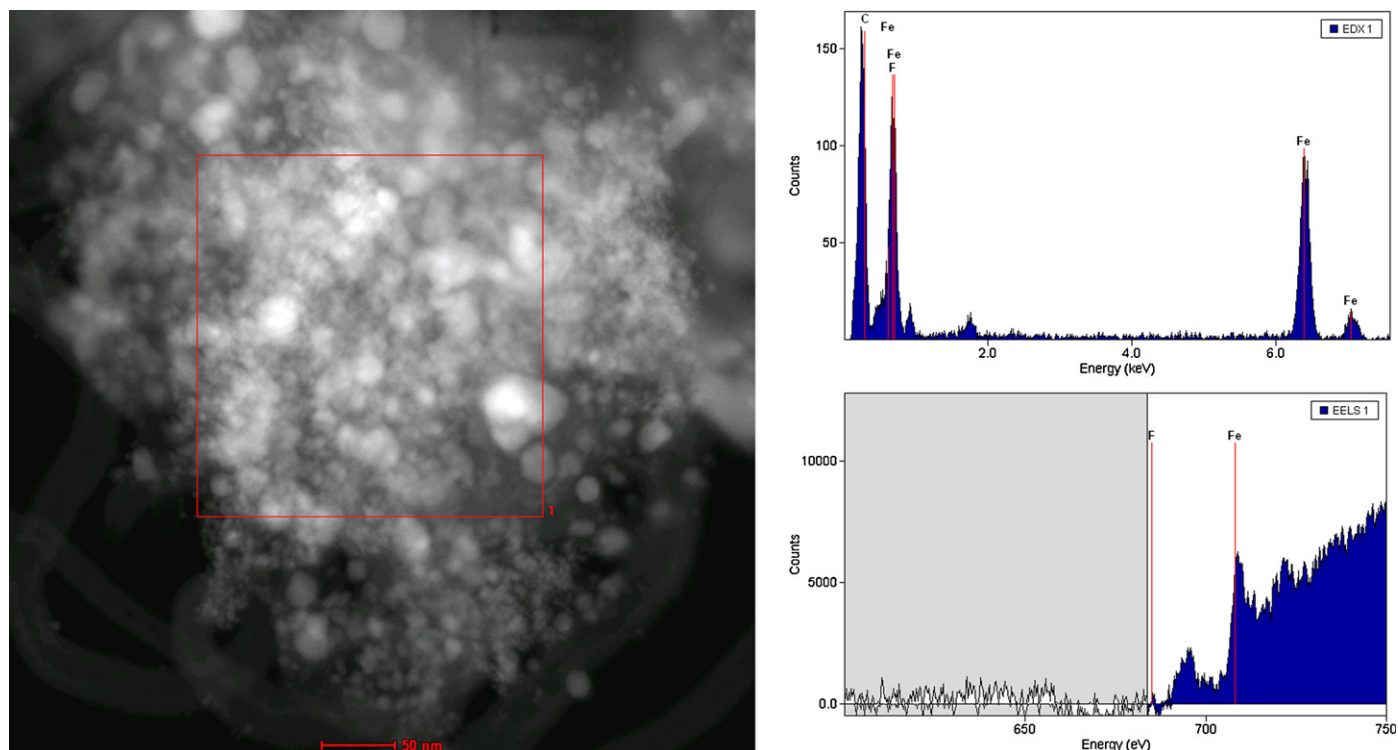
Fig. 6. HAADF-STEM reference image of **1** (left), and EELS and EDX spectra (right) of the selected area showing strong C, Fe and F signals.
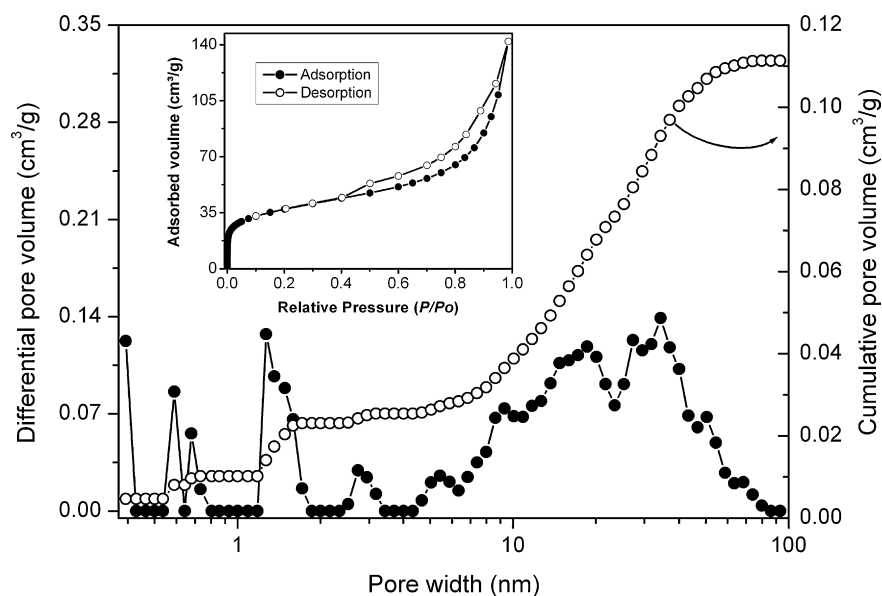

Fig. 7. Cumulative pore volume and differential pore volume as a function of pore width of **1** measured at $-196\,°C$. Inset: N_2 isotherm.

After cycled at higher current densities, the discharge capacity went back nearly to the original value ($220\,mAh\,g^{-1}$) as the current density was reduced again to the initial value ($20.8\,mA\,g^{-1}$). In addition, the composite electrode cycled between 4.3 and 1.3 V at a current density of $1420\,mA\,g^{-1}$ exhibits good cyclic performance with a reversible specific capacity of $55\,mAh\,g^{-1}$, and retained its capacity over 90% after 100 cycles (figure not shown). The rate performance of **1** is reasonably good for such kind of conversion materials having intrinsically low electrical conductivity. The performance of **1** can be attributed to its morphology, especially the networking of nanotubes with nano-granular region containing active materials that help providing fast electronic and ionic transports.

The binder-free cathode **1** exhibits an improved specific capacity of $60\,mAh\,g^{-1}$ compared to the previous [Fe/LiF/C] nanocomposite cathode (with binder) under identical condition, which is approximately equivalent to one third of the reversible capacity of the previous nanocomposite. The significant increase of the specific capacity may some extent be attributed to the presence of relatively higher quantity of reactive Fe species in **1** than that of the previous nanocomposite. The Mössbauer data of **1** show an increase in overall iron content (α-Fe and Fe–C $\sim 61\%$) other than Fe_3C form ($\sim 39\%$). We assume that both the crystalline and the amorphous iron phases of **1** might have participated in the electrochemical reaction. A detailed Mossbauer investigation is required for further under-
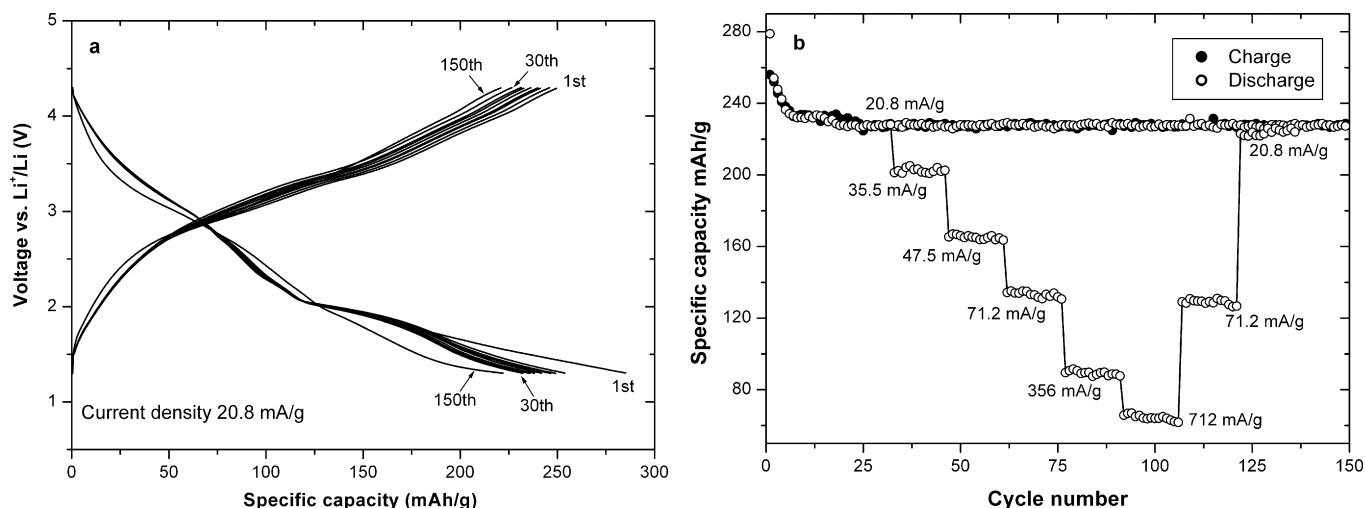
Fig. 8. Electrochemical characterization of **1**. (a) Galvanostatic charge/discharge voltage vs. specific capacity profile. (b) Specific capacity vs. cycle number at various current densities. The nanocomposite was cycled between 4.3 and 1.3 V.
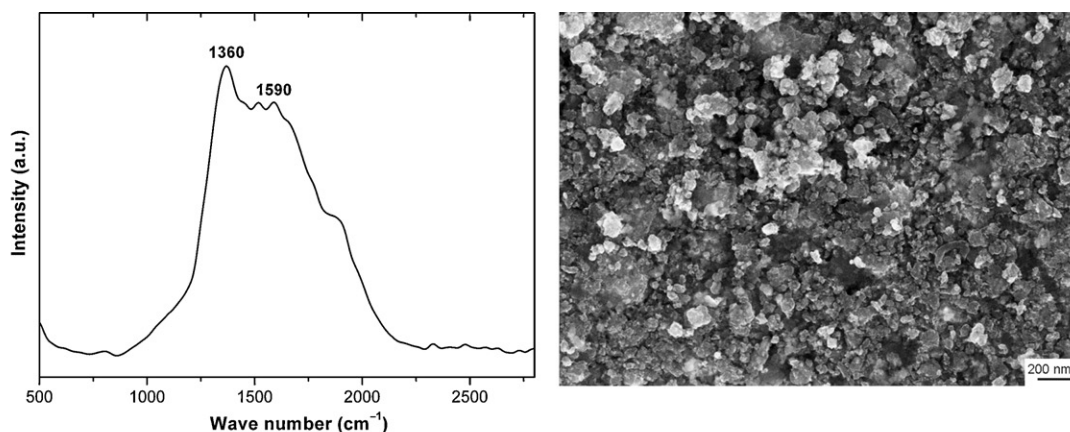

Fig. 9. Characterization of nanocomposite **2**. Raman spectrum (top left), SEM image (top right), and TEM images (bottom) showing iron particles embedded in the carbon matrix. Most of the graphitic structure is highly disordered and typically no well-defined graphitic layers are visible around the metal nanoparticles.

standing of this process. However, both composites exhibit equally good cyclic stability and rate capability performances, irrespective of their preparation conditions. The cyclic stability and rate capability behaviors can be associated to the morphology of the electrode materials. Since both the original and the modified composites possess essentially similar morphologies, their cyclic stability and rate performances remain unchanged. In order to correlate the morphology of the material and cyclic stability, nanocomposite **1** was ball milled under moderate conditions to change its morphology without altering its composition. The structure/morphology and

electrochemical performance of the ball milled nanocomposite **2** was studied and compared with **1**.

The XRD analysis of **2** (Supplementary information Fig. S3) exhibits a similar pattern as of **1**. All of the reflection peaks can be indexed to C, Fe, Fe$_3$C and LiF phases. However, the Fe and LiF reflections were substantially broadened and merged with each other. In addition, the peak at 26.4° corresponding to the graphitic carbon is completely broadened due to the ball-milling which created more disordered graphitic layers and some amorphous carbon materials. Raman spectrum of **2** (Fig. 9) corroborates
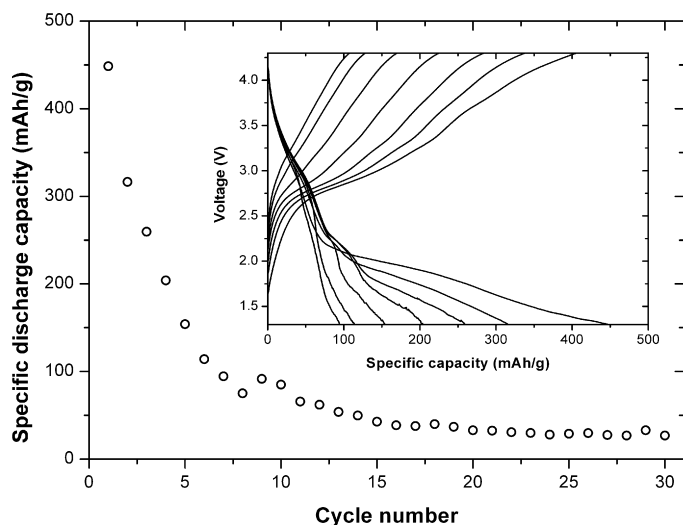
Fig. 10. Electrochemical characterization of **2**. Specific capacity vs. cycle number profile at 20.8 mA g^{-1}. The nanocomposite was cycled between 4.3 and 1.3 V. Inset: galvanostatic charge/discharge voltage vs. specific capacity profile.

well the XRD analysis. The intensity of the disordered graphitic band at 1360 cm^{-1} increased and the intensity ordered G-band at 1590 cm^{-1} decreased significantly. The SEM image of **2** reveals that the typical entangled nanotube structure was completely destroyed by ball-milling. Closer analysis of the material by high-resolution TEM shows that iron rich particles were embedded mostly in a carbonaceous matrix. The core shell type structures with an iron rich core and well-defined graphitic layers around it, as observed in **1**, disappeared almost completely. In addition, STEM images of **2** showed a few elongated metal particles due to the impact of ball milling (Supplementary information Fig. S4). HAADF-STEM in combination with local EDX analyses (Supplementary information Fig. S5) revealed a rather uniform distribution of all elements present throughout the aggregates as seen before for **1**. In addition, the results of EDX (SEM mode) and elemental analysis were in good agreement with those of **1**, suggesting that the elemental composition of **2** was not changed. Compound **2** exhibits similar N$_2$ adsorption–desorption isotherm (Supplementary information Fig. S6) as of **1**. The sample has micro- and mesoporous volumes of 0.038 and 0.043 cm^3 g^{-1}, respectively. The PSD calculated from DFT model is very broad and with a mean mesopore size of about 35 nm. When compared to **1**, the micropore volume of **2** was increased and mesopore volume was decreased significantly due to ball-milling. The BET surface area was 89 m^2 g^{-1}, which is considerably lower than that of **1**.

Fig. 10 shows the electrochemical performance of the nanocomposite electrode **2** cycled between 1.3 and 4.3 V versus lithium at a current density of 20.8 mAg^{-1}. The discharge capacities at the first and tenth cycles are 448 and 92 mAh g^{-1}, respectively, and the corresponding capacity loss was about 80%. Despite the higher initial capacities, composite **2** undergoes rapid loss of capacity with cycling similar to the behavior observed in most metal fluoride nanocomposites prepared by ball-milling method [13–16]. The irreversible capacity loss is most likely due to loss of electrical contact between active materials and conductive matrix. On the contrary, **1** exhibited excellent cyclic stability, which suggests that the carbon framework plays a dual role by integrating the active materials as well as networking good electrical contact.

4. Conclusions

A simple rotating quartz tube setup has been developed to prepare [Fe/LiF/C] nanocomposite, from pyrolysis of a ferrocene/LiF

mixture. As a result homogeneity and uniformity of the material in terms of mixing of components were greatly improved. The nanocomposite consisted of well-defined carbon nanotubes and core shell-type graphite structures where iron-rich nanoparticles were encapsulated. As the cathode materials for lithium-ion battery, the nanocomposite electrode showed enhanced electrochemical performance with the reversible specific capacity of 230 mAh g^{-1} at 20.8 mA g^{-1} in the voltage range of 1.3–4.3 V at room temperature. The simple synthetic modification of **1** resulted in a capacity enhancement of 60 mAh g^{-1} compared to the previous nanocomposite (170 mAh g^{-1}). Composite **1** exhibited a good cyclic stability and rate capability performances which can be attributed to its morphology; interconnection between the nano−tubes and the nanogranular regions containing active materials which has efficiently improved the electronic and ionic transports in the electrode. Efforts are currently underway to optimize the nanocomposite to improve further the capacity of the system.

Appendix A. Supplementary data

Supplementary data associated with this article can be found, in the online version, at doi:10.1016/j.jpowsour.2011.03.007.

References

[1] J.M. Tarascon, M. Armand, Nature 414 (2001) 359.
[2] M.S. Whittingham, Chem. Rev. 104 (2004) 4271.
[3] K. Kang, Y.S. Meng, J. Bréger, C.P. Grey, G. Ceder, Science 311 (2006) 977.
[4] P.G. Bruce, B. Scrosati, J.M. Tarascon, Angew. Chem. Int. Ed. 47 (2008) 2930.
[5] A.K. Padhi, K.S. Nanjundaswamy, J.B. Goodenough, J. Electrochem. Soc. 144 (1997) 1188.
[6] Y.J. Lee, H. Yi, W.J. Kim, K. Kang, D.S. Yun, M.S. Strano, G. Ceder, A.M. Belcher, Science 324 (2009) 1051.
[7] Y.G. Guo, J.S. Hu, L.J. Wan, Adv. Mater. 20 (2008) 2878.
[8] P. Poizot, S. Laruelle, S. Grugeon, L. Dupont, J.M. Tarascon, Nature 407 (2000) 496.
[9] P.L. Taberna, S. Mitra, P. Poizot, P. Simon, J.M. Tarascon, Nat. Mater. 5 (2006) 567.
[10] Y. Li, B. Tan, Y. Wu, Nano Lett. 8 (2008) 265.
[11] N. Pereira, M. Balasubramanian, L. Dupont, J. McBreen, L.C. Klein, G.G. Amatucci, J. Electrochem. Soc. 150 (2003) 1118.
[12] H. Li, W. Li, L. Ma, W. Chen, J. Wang, J. Alloys Compd. 471 (2009) 442.
[13] F. Badway, N. Pereira, F. Cosandey, G.G. Amatucci, J. Electrochem. Soc. 150 (2003) A1209.
[14] H. Li, G. Richter, J. Maier, Adv. Mater. 15 (2003) 736.
[15] F. Badway, F. Cosandey, N. Pereira, G.G. Amatucci, J. Electrochem. Soc. 150 (2003) A1318.
[16] M. Nishijima, I.D. Gocheva, S. Okada, T. Doi, J.-I. Yamaki, T. Nishida, J. Power Sources 190 (2009) 558.
[17] W. Wu, X. Wang, X. Wang, S. Yang, X. Liu, Q. Chen, Mater. Lett. 63 (2009) 1788.
[18] N. Yamakawa, M. Jiang, B. Key, C.P. Grey, J. Am. Chem. Soc. 131 (2009) 10525.
[19] T. Li, L. Li, Y.L. Cao, X.P. Ai, H.X. Yang, J. Phys. Chem. C 114 (2010) 3090.
[20] C. Li, L. Gu, S. Tsukimoto, P.A. van Aken, J. Maier, Adv. Mater. 22 (2010) 3650.
[21] S.-W. Kim, D.-H. Seo, H. Gwon, J. Kim, K. Kang, Adv. Mater. (2010), doi:10.1002/adma.201002879.
[22] H. Arai, S. Okada, Y. Sakurai, J. Yamaki, J. Power Sources 68 (1997) 716.
[23] H. Li, P. Balaya, J. Maier, J. Electrochem. Soc. 151 (2004) A1878.
[24] R. Prakash, A.K. Mishra, A. Roth, C. Kübel, T. Scherer, M. Ghafari, H. Hahn, M. Fichtner, J. Mater. Chem. 20 (2010) 1871.
[25] R. Prakash, C. Kübel, M. Fichtner, in: G. Wicks, et al. (Eds.), Materials Challenges in Alternative and Renewable Energy, Ceram. Trans., vol. 224, John Wiley & Sons Inc., New Jersey, 2011, pp. 173–182.
[26] P.A. Webb, C. Orr, Analytical Methods in Fine Particle Technology, 1st ed., Micromeritics Instrument Corporation, Norcross, 1997.

[27] S. Brunauer, P.H. Emmett, E. Teller, J. Am. Chem. Soc. 60 (1938) 309.
[28] S. Yin, P.K. Shen, S. Song, S.P. Jiang, Electrochim. Acta 54 (2009) 6954.
[29] S. Lefrant, I. Baltog, M. Baibarac, J. Schrieber, O. Chauvet, Phys. Rev. B 65 (2002) 235401.
[30] E. Bauer-Grosse, C.G. Le, Philos. Mag. B 56 (1987) 485.
[31] N.N. Greenwood, T.C. Gibb, Mossbauer Spectroscopy, Chapman and Hall Ltd., London, 1971, p. 318.
[32] K.S.W. Sing, D.H. Everett, R.A.W. Haul, L. Moscou, R.A. Pierotti, J. Rouquerol, T. Siemieniewska, Pure Appl. Chem. 57 (1985) 603.